Materials Advances

ROYAL SOCIETY OF CHEMISTRY

PAPER

View Article Online
View Journal | View Issue

Cite this: *Mater. Adv.*, 2024, 5, 2411

High-efficiency ITO-free organic solar cells through top illumination†

Yu-Ching Huang, *[abc] Chih-Chien Lee,[d] Yung-Yuan Lee,[d] Ssu-yung Chung,[ab] Hui-Chieh Lin,[a] Uma Kasimayan,[a] Chia-Feng Li[b] and Shun-Wei Liu *[ae]

Received 9th December 2023,
Accepted 23rd January 2024

DOI: 10.1039/d3ma01103h

rsc.li/materials-advances

Organic photovoltaics (OPVs) hold great promise for commercialization due to their potential to produce high-performance, and flexible products in a cost-effective and scalable way. Beyond achieving high power conversion efficiency (PCE), the ability to maintain device stability under atmospheric conditions is important for the practical application of flexible OPVs. Our primary objective is to significantly enhance the stability of OPVs by incorporating flexible layers, eliminating unstable materials, and adopting an ITO-free approach. We developed a top-illuminated crumpled OPV architecture by utilizing parylene and Ag layer as the electrode materials. To enhance the PCE of ITO-free OPVs, we have incorporated the electron transport layer, PFN-Br, followed by the deposition of the PM6:Y6 active layer. An intriguing breakthrough emerged in the form of MoO_3/Ag/WO_3, serving as an innovative transparent electrode and replacing the conventional ITO electrode. The ultimately crumpled OPV exhibited superior PCE and attained a high power-per-weight of 31.07 W g^{-1}. Furthermore, the ITO-free device exhibited excellent stability during dark storage (T95 ~ 1000 hours) and light soaking conditions (T93 ~ 48 hours). Remarkably, even after 48 hours of continuous light soaking, the freestanding crumpled OPVs maintained the PCE at 93% of its initial value, showcasing excellent photostability.

Introduction

Organic photovoltaics (OPVs) have garnered significant attention due to their advantages, including light weight,[1,2] flexibility,[3,4] semi-transparency,[5,6] low manufacturing cost,[7,8] and ease of large-area processing.[9,10] In recent years, OPVs fabricated from non-fullerene acceptors (NFAs) have been extensively studied for their potential to achieve high power conversion efficiency (PCE).[11–13] NFAs can be synthesized by molecular design engineering to exhibit a broad absorption range from 400 nm to 900 nm. Moreover, this approach effectively mitigates radiative and non-radiated energy losses, leading to significantly enhanced short-circuit density (J_{sc}) and open-circuit voltage (V_{oc}).[14] The PCE of NFA-based OPVs has experienced remarkable improvement, surpassing 19%, thus showcasing substantial potential for commercialization. With the great progress in OPV technology, leveraging the inherent advantages compared to other PV systems becomes a strategic approach in unlocking their commercial success within niche markets.[15] Recently, the portable power supplies have gained increasing interest for various applications, including electronic skin, internet of things (IoT) sensors, and drones.[16–20] In such applications, the key requirements revolve around the need for light weight and mechanical flexibility, both of which are the superior advantages offered by OPV over other PV technologies. Despite the numerous advantages offered by conventional rigid or flexible OPV devices, their full potential is often hindered by the use of thick glass or plastic substrates, which add unnecessary weight to the devices. To overcome this limitation, the emergence of ultra-flexible (or ultra-thin) OPVs offer a potential solution, as they eliminate the weight issue and allow the benefits of the technology to be used more efficiently. The ability of these OPVs to fit seamlessly onto the surface of any shape of the object makes them ideal for integration into a wide range of cutting-edge applications, including IoT and aeronautic devices. A noteworthy example from a previous literature report demonstrates that by attaching ultra-flexible OPVs to the wings of drones with minimal added weight, their flight time could

[a] *Organic Electronics Research Center, Ming Chi University of Technology, New Taipei City 24301, Taiwan. E-mail: huangyc@mail.mcut.edu.tw, swliu@mail.mcut.edu.tw*
[b] *Department of Materials Engineering, Ming-Chi University of Technology, New Taipei City, 24301, Taiwan*
[c] *Department of Chemical and Materials Engineering, College of Engineering, Chang Gung University, Taoyuan 33302, Taiwan*
[d] *Department of Electronic Engineering, National Taiwan University of Science and Technology, Taipei City, 106335, Taiwan*
[e] *Department of Electronic Engineering, Ming Chi University of Technology, New Taipei City 24301, Taiwan*

† Electronic supplementary information (ESI) available: The detailed calculation of power-per-weight is provided. In addition, the attached video serves to illustrate the seamless removal of our device from the ITO substrate. See DOI: https://doi.org/10.1039/d3ma01103h

potentially be significantly extended.[1] As a result, the potential of ultra-flexible OPVs in revolutionizing diverse industries is generating high anticipation.

In 2015, Jean *et al.* demonstrated that the *in situ* vapor-phase growth technique could produce ultrathin, flexible solar cells (2.3 mm) based on perylene-C films with performance comparable to solar cells deposited on glass substrates. These flexible cells can be seamlessly attached to various surfaces for additional solar power.[21] Until now, diverse strategies have been explored to enhance the stability of flexible OPVs, with the incorporation of stable materials into the active layer proving effective in increasing storage stability. Another approach involves the integration of an ultraviolet (UV) filter film, which has emerged as a crucial method for boosting the photostability of flexible OPVs.[22] A recent notable breakthrough features a flexible OPV with an impressive PCE of 16.1%.[23] This device, designed in a biomimetic leaf-like structure to efficiently capture light, managed to maintain around 75% of its initial efficiency after being stored for 60 hours in ambient air. Furthermore, OPVs have achieved remarkable efficiencies of up to 19.76% for single-junction devices and 20.2% for tandem devices.[24,25] These figures essentially meet the threshold for commercial viability within the photovoltaic industry. The attainment of long-term stability remains a significant challenge hindering the widespread adoption of OPVs. Recent advancements, exemplified by Xiong *et al.*, ultra-flexible OPV boasting a 15.8% PCE and a remarkable power-per-weight of 33.8 W g^{-1}, demonstrate the potential of this technology.[26] Conversely, a stabilized PCE of 15.5% was attained, along with power-per-weight of 32.07 W g^{-1} at a weight of 4.83 g m^{-2}, demonstrating notable stability when stored in an N_2-filled glove box. This storage approach led to the PCE retaining over 95% of its initial efficiency even after an extended duration of 1000 hours.[27] A noteworthy contribution by X. Zheng *et al.* revealed that the ultra-flexible OPVs maintained 97% PCE throughout 5000 consecutive compression–release deformation cycles. This performance was accompanied by an excellent power-per-weight of 39.72 W g^{-1}, achieved at a weight of 4.36 g m^{-2}.[1] Ultra-flexible OPVs must withstand extreme bending, necessitating electrodes with superior mechanical flexibility, and their fabrication is intricate due to the susceptibility of easily wrinkled ultra-thin substrates. Consequently, although the efficiency of ultra-flexible OPVs has shown progress, it still trails behind that of conventional flexible OPVs, and there is a relative lack of research into stability of ultra-flexible OPVs in particular.

The typical structure of the OPVs consists of a transparent electrode, an electron or hole transport layer (ETL or HTL), an active layer, an interfacial layer, and a metal electrode. Indium tin oxide (ITO) is a widely used transparent conductive electrode in OPVs due to its high optical transparency and electrical conductivity.[28,29] However, the realization of ultra-flexible OPVs faces significant challenges because of several drawbacks associated with the commonly used ITO material. These drawbacks include high manufacturing cost, brittleness, and long-term stability.[30,31] Subsequently, the HTL, typically composed of poly(3,4-ethylenedioxythiophene)–poly(styrenesulfonate) (PEDOT:PSS) in the device process, often exhibits a limited lifetime. This can be attributed to its inclination to interact with the ITO electrode and its vulnerability to humidity due to its acidic and high hygroscopic nature. As a result, it can lead to the formation of shunts and defects, particularly when utilized as an electrode in solar cells.[32,33] While attempts to achieve stability have been made through thin polymer encapsulation layers, these efforts are hindered by inadequate barrier properties. Furthermore, the chemical composition of the metal oxide in HTLs can undergo alteration during annealing, thereby causing obvious device degradation. To address this, alternative transparent electrodes to ITO have been broadly studied, such as metal nanowires, highly conductive polymer, graphene, and thin metal layer.[32,34–40] Among these technologies, the thin metal layer exhibits the advantages of low manufacturing cost, high mechanical flexibility, and high conductivity. In addition to conventional architecture, the top-illuminated device structure has emerged as an effective way towards highly efficient and stable ITO-free OPVs. One of the key challenges in implementing top-illuminated OPVs lies in the development of transparent top electrodes capable of facilitating efficient light transmission while maintaining high electrical conductivity.[41–43] This is crucial for advancing the potential of top-illuminated OPVs and realizing their significant benefits in the field of OPVs.

In this study, we present a top-illuminated ITO-free crumpled OPV structure, utilizing flexible parylene and an Ag layer serving as the electrode. To achieve lightweight characteristics, we incorporated the poly(9,9-bis(3′-(*N*,*N*-dimethyl)-*N*-ethylammoinium-propyl-2,7-fluorene)-*alt*-2,7-(9,9-dioctylfluorene))dibromide polymer (PFN-Br) as the ETL, with the active layer subsequently deposited on it. Addressing the challenge of replacing the conventional ITO transparent electrode, we employed MoO_3/Ag/WO_3 as the alternative transparent electrode. In order to enhance the stability of the crumpled OPV, we applied a deposition of Al_2O_3 fully covering the entire crumpled OPV. Remarkably, this crumpled OPV demonstrated impressive properties, boasting a high power-per-weight ratio of up to 31.07 W g^{-1} and excellent stability with respect to under dark (T95 $\sim$ 1000 hours) and light illumination (T93 $\sim$ 48 hours) conditions.

Experimental section

Materials

The flexible parylene substrate was purchased from Taiwan Innova Efficiency Inc. The ETL, PFN-Br, was obtained from Sigma-Aldrich. Additionally, the donor materials, poly[(2,6-(4,8-bis(5-(2-ethylhexyl-3-fluoro)thiophen-2-yl)-benzo[1,2-*b*:4,5-*b*′]dithiophene))-*alt*-(5,5-(1′,3′-di-2-thienyl-5′,7′-bis(2-ethylhexyl)benzo[1′,2′-*c*:4′,5′-*c*′]dithiophene-4,8-dione)] (PM6), and NFA material, 2,2′-((2*Z*,2′*Z*)-((12,13-bis(2-ethylhexyl)-3,9-diundecyl-12,13-dihydro-[1,2,5]thiadiazolo[3,4-*e*]thieno[2″,3″:4′,5′]thieno[2′,3′:4,5]pyrrolo[3,2-*g*]thieno[2′,3′:4,5]thieno[3,2-*b*]indole-2,10-diyl)bis(methanylylidene))bis(5,6-difluoro-3-oxo-2,3-dihydro-1*H*-indene-2,1-diylidene))dimalononitrile (Y6), were supplied by 1-Materials. The solvents, MoO_3 and WO_3 were purchased from Sigma-Aldrich.

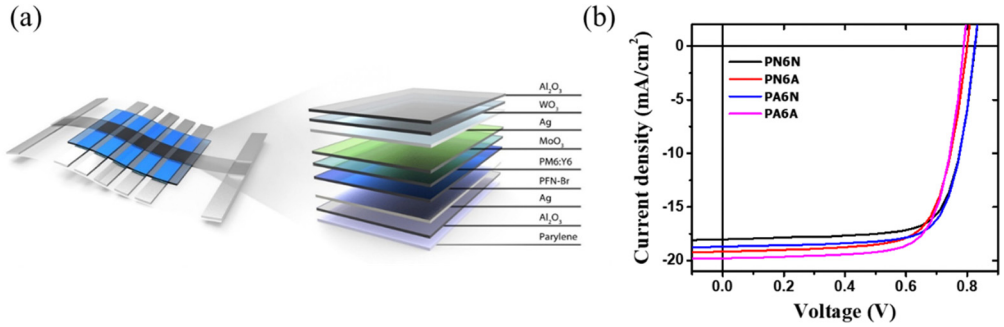

Fig. 1 (a) The lightweight and crumpled device layout and structure of this work. (b) *J*–*V* curves of OPV performance different annealing conditions for PFN-Br and PM6:Y6 Layers. The PM6:Y6 layer is examined without (PN6N) and with (PN6A) thermal annealing of 100 °C for 10 min, while the PFN-Br layer maintains a constant temperature of 100 °C for 1 min with (PA6N) and without (PA6A) annealing of PM6:Y6 of 100 °C at 10 min.

Device preparation

We fabricated the OPV devices using an inverted structure. Fig. 1a shows the crumpled device layout and structure. The preparation of our crumpled OPV involved the following device structure: parylene (2 μm)/Al_2O_3 (30 nm)/Ag (100 nm)/PFN-Br (10 nm)/PM6:Y6 (100 nm)/MoO_3 (10 nm)/Ag (12 nm)/WO_3 (30 nm)/Al_2O_3 (30 nm). The parylene films are commonly used for crumpled OPV substrates, where they are deposited on the glass substrate and subsequently peeled off after the entire device has been fabricated. Firstly, the glass was ultrasonically cleaned with acetone and isopropanol in a sequence. Parylene films were grown on clean glass by chemical vapor deposition (CVD). Then, atomic layer deposition (ALD) was used to deposit Al_2O_3 on the parylene films. A 100 nm thick silver film was deposited on the Al_2O_3 as the bottom electrode using thermal evaporation. The ETL solution composed of PFN-Br (1 mg ml^{-1}) obtained by dissolving in methanol and spin-coating at 3000 rpm for 30 s. The photoactive layer solution consisted of PM6 and Y6 (1 : 1.5, w/w) dissolved in chloroform, which was spin-coated at 1500 rpm for 60 s in a glove box. PFN-Br and the active layer were annealed under different annealing conditions. Then, MoO_3, Ag, and WoO_3 were sequentially deposited as a rear transparent electrode onto a photoactive layer through thermal evaporation, and Al_2O_3 was deposited as the encapsulation layer for crumpled OPVs by using ALD. In this study, we have listed the structure and name of the used devices as follows:

Device 1: glass/parylene/Al_2O_3/Ag/PFN-Br/PM6:Y6/MoO_3/Ag/WO_3

Device 2: glass/parylene/Al_2O_3/Ag/PFN-Br/PM6:Y6/MoO_3/Ag/WO_3/Al_2O_3

Device 3: parylene/Al_2O_3/Ag/PFN-Br/PM6:Y6/MoO_3/Ag/WO_3/Al_2O_3

Device 4: glass/parylene/Al_2O_3/Ag/PFN-Br/PM6:Y6/MoO_3/Ag/WO_3/glass

Table 1 Performance of OPVs prepared using PFN-Br and PM6:Y6 layers under different annealing conditions (Device 1[a]). These values are for the highest PCE of the devices, and the average data are obtained from 20 devices in the brackets

Device	V_{oc} (V)	J_{sc} (mA cm^{-2})	FF (%)	PCE (%)
PN6N	0.83 (0.82 ± 0.00)	18.03 (17.9 ± 0.22)	74.11 (72.06 ± 1.71)	11.03 (10.59 ± 0.27)
PN6A	0.80 (0.79 ± 0.01)	19.15 (19.03 ± 0.30)	72.12 (71.55 ± 0.69)	11.05 (10.74 ± 0.24)
PA6N	0.82 (0.82 ± 0.00)	18.68 (18.26 ± 0.29)	74.27 (73.37 ± 1.07)	11.45 (11.03 ± 0.31)
PA6A	0.79 (0.79 ± 0.01)	19.80 (19.38 ± 0.41)	73.52 (71.35 ± 2.42)	11.48 (10.92 ± 0.48)

[a] Device structure (Device 1): glass/parylene/Al_2O_3/Ag/PFN-Br/PM6:Y6/MoO_3/Ag/WO_3.

Characteristic analysis

The PCE of devices was measured under AM 1.5G illumination (100 mW cm^{-2}) by using a solar simulator (SS-X100R, Enlitech), and the external quantum efficiency (EQE) was measured by solar cell spectral response measurements (QE-R3011, Enlitech). The thin film morphology was characterized using atomic force microscopy (AFM) measurements (Innova, Bruker). The optical properties, including absorption and transmission, were evaluated using a UV-Vis spectrometer (JASCO, V-770). The charge extraction time and charge recombination time were determined through transient photovoltage (TPV) and transient photocurrent (TPC) measurements using a Paios 4.0 instrument (FLUXiM AG, Switzerland). Device stability measurements were conducted using a voltage source meter (Keithley 2410) under a simulated AM 1.5G illumination solar simulator (Newport LSH-7320) with an irradiance of 100 mW cm^{-2}. The testing environment was maintained at 25 °C with humidity between 40 and 50%.

Results and discussion

To achieve flexibility and lightweight device, a parylene film is widely utilized as the flexible substrate. However, the weak thermal tolerance of flexible substrate limits the choice of materials. To overcome this thermal limitation, we have adopted PFN-Br as the ETL for our flexible devices. PFN-Br is characterized by its solubility in methanol, with the significant advantage of processing temperature below 100 °C. Additionally, improving wettability by utilizing solvent systems with low surface tension is important to reduce the interfacial defects.[44]

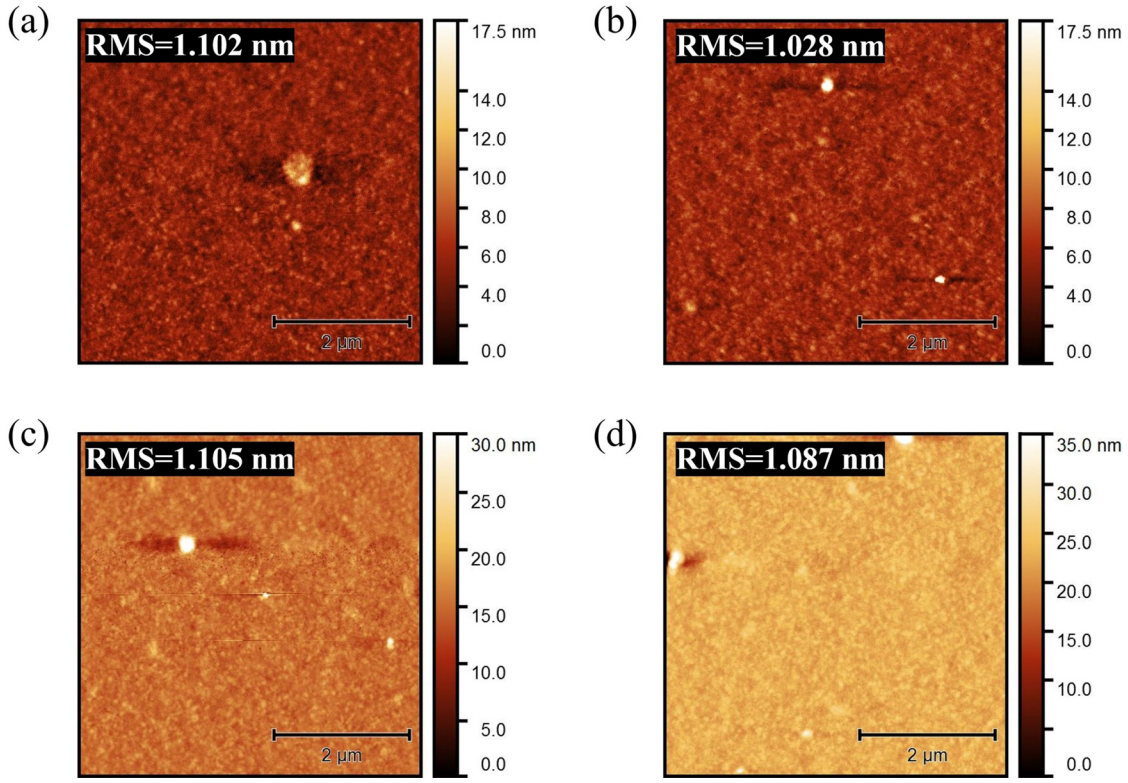

Fig. 2 AFM images of (a) PN6N, (b) PN6A, (c) PA6N, and (d) PA6A films using PFN-Br and PM6:Y6 layers under different annealing conditions.

Moreover, we also used different thermal treatments for PFN-Br and active layer to improve the PCE of the devices. Table 1 provides insight into the performance of Device 1 under different annealing conditions applied to the PFN-Br and

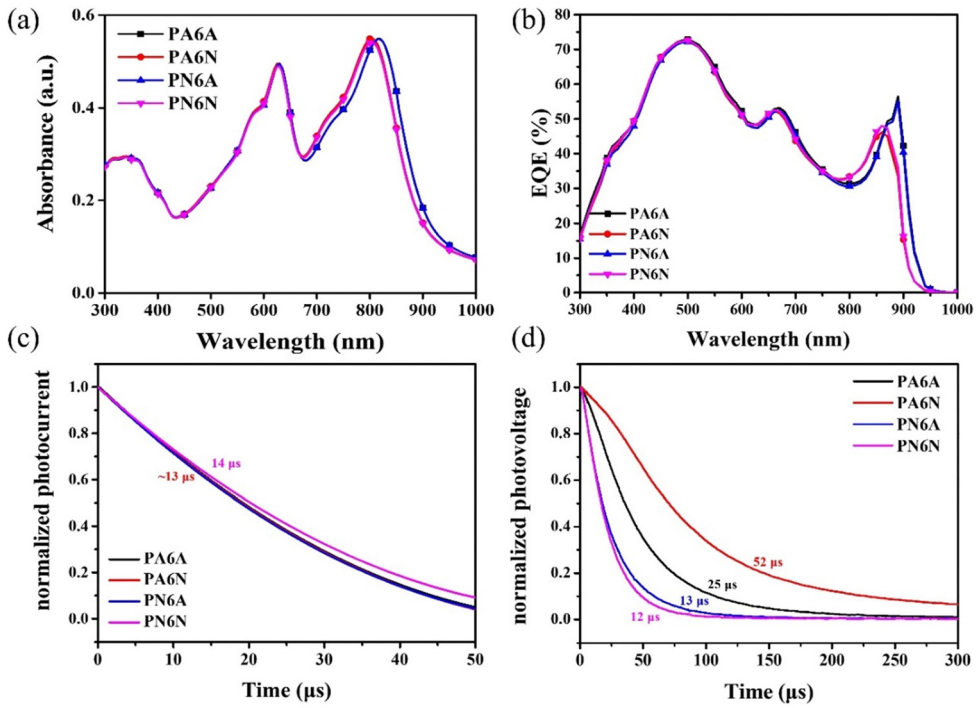

Fig. 3 (a) Absorption spectra (b) external quantum efficiency (EQE) (c) transient photocurrent and (d) transient photovoltage measurements of PA6A, PA6N, PN6A, and PN6N films using PFN-Br and PM6:Y6 films under different annealing conditions.

PM6:Y6 layers. Specifically, we examined the PM6:Y6 layer in two conditions: one without thermal annealing (PN6N) and another with thermal annealing at 100 °C for 10 minutes (PN6A). In parallel, the PFN-Br layer was maintained at a constant temperature of 100 °C for 1 minute for two different configurations: one without annealing (PA6N) and another with annealing of the PM6:Y6 layer at 100 °C for 10 minutes (PA6A). Fig. 1b depicts the *J*–*V* curves, while Table 1 provides a summary of the corresponding PCE performance enhancements resulting from various thermal annealing processes applied to PFN-Br and PM6:Y6, respectively.

Fig. 2 shows the AFM images of the active layer under different thermal annealing conditions of (a) PN6N, (b) PN6A, (c) PA6N, and (d) PA6A, respectively. The results show that the thermal annealing conditions did not have much effect on the surface morphology of the active layer films, with little discernible alteration in the surface roughness. Based on the thermal annealing treatment, it appears that the PCE performance did not change significantly, achieving average values of 10.59%, 10.74%, 11.03%, and 10.92% for PN6N, PN6A, PA6N, and PA6A, respectively as illustrated in Table 1. Regarding the performance, the average PCE of PN6N devices increased from 10.59% to 11.03% after thermal annealing of PFN-Br at 100 °C for 10 min. This enhancement in the PCE can be attributed to the improvement of J_{sc} from 17.9 mA cm^{-2} to 18.26 mA cm^{-2}.

Fig. 3a shows the absorption spectra of PA6A, PA6N, PN6A, and PN6N, respectively. Compared to the PN6N film, there is no significant difference in the absorption of either annealed layer, except for the PN6A film showing a slight red shift. This result implies that the absorption behavior of the active layers is not significantly changed by the annealing. In Fig. 3b, EQE of the PN6A device was red-shifted and slightly increased at 900 nm, consistent with the results from the absorption spectrum. According to the UV-Vis and EQE results, the slight improvement in J_{sc} implied that the annealing process probable enhancing the light-harvesting ability of the devices. However, the increase in J_{sc} does not bring about a significant benefit in terms of PCE, as other photovoltaic parameters, especially V_{oc}, decrease accordingly. Notably, the average PCE of the PA6A devices reached a value of 10.92%, and the highest PCE of 11.48% was achieved using the thermal-annealed ETL and active layer. To examine the impact of the annealing effect of PFN-Br on charge extraction, TPC measurements were carried out, and the results are presented in Fig. 3c. The charge extraction time for the PA6N device was slightly lower, around 13 μs compared to the PN6N device, which had a charge extraction time of approximately 14 μs. This indicates that the extraction ability of PFN-Br did not change significantly during thermal annealing. In Fig. 3d, TPV measurement was examined to assess the suppressing effect of the ETL on the charge recombination. The PA6A device exhibited an extended charge recombination lifetime of 25 μs, while the PN6A device had a charge recombination of lifetime of 13 μs. This implied a reduction in the charge loss at the interface between thermal-annealed PFN-Br and PM6:Y6, contributing to the improved

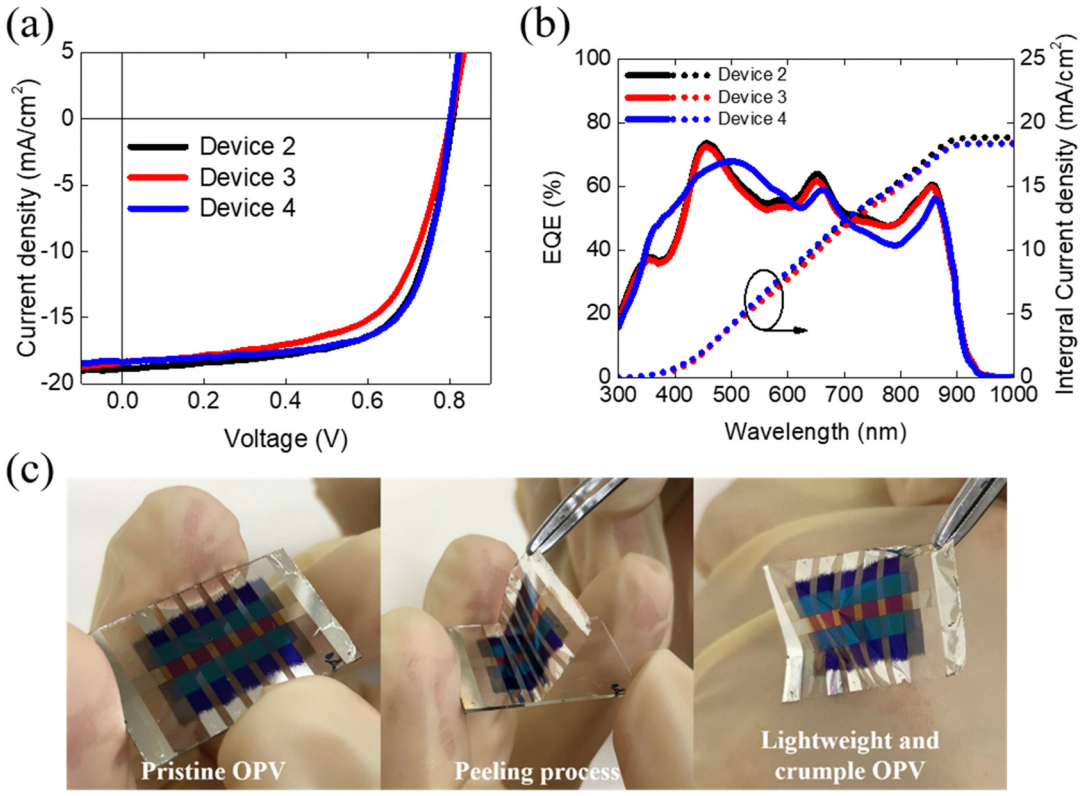

Fig. 4 (a) *J*–*V* characteristic and (b) external quantum efficiency of OPV devices based on the structures of Device 2, Device 3, and Device 4. (c) The demonstration photos illustrate the step-by-step process of using the peeling method to obtain lightweight and crumpled OPV devices.

Table 2 Device performances of OPVs based on PM6:Y6 active layer with different device structures. The standard deviation values for each parameter are calculated based on measurements from five devices

Device type	V_{oc} (V)	J_{sc} (mA cm^{-2})	FF (%)	PCE (%)	Int. J_{sc} (mA cm^{-2})	P_{max} (mW)
Device 2	0.79 (0.78 ± 0.00)	18.17 (17.79 ± 0.14)	66.79 (64.22 ± 2.96)	9.70 (8.95 ± 0.54)	18.18 17.89	0.39 0.36 ± 0.02
Device 3	0.80 (0.81 ± 0.00)	18.36 (17.84 ± 0.53)	61.99 (60.08 ± 1.91)	9.26 (8.75 ± 0.51)	18.37 17.85 ± 0.74	0.37 0.35 ± 0.02
Device 4	0.81 (0.81 ± 0.00)	16.70 (16.30 ± 0.16)	71.82 (71.19 ± 0.83)	9.75 (9.42 ± 0.21)	16.73 16.45	0.39 0.38 ± 0.01

performance observed in the PA6A device. In addition, the PA6A devices had a shorter recombination lifetime than the PA6N, suggesting that the annealing of the photoactive layer may lead to a deterioration of the charge recombination at the interface, thus leading to a lower V_{oc}. Both PA-based devices showed longer recombination lifetimes compared to the PN-based devices, suggesting that ETL annealing is clearly beneficial in reducing charge recombination losses.

Fig. 4a displays the *J–V* curves of the Device 2, Device 3 and Device 4, and the corresponding photovoltaic characteristics are listed in Table 2. The reference device has a structure of Device 4, with a PCE is 9.42%, a V_{oc} of 0.81 V, a J_{sc} of 16.30 mA cm^{-2}, and FF of 71.19%. The electrode, Al_2O_3/Ag, was deposited on the parylene/Glass. Additionally, the top transparent electrode, MoO_3/Ag/WO_3/Al_2O_3 were deposited on the active layer for light illumination. The resulting PCE of the top-illuminated device is 8.95%, with a V_{oc} of 0.78 V, a J_{sc} of 17.79 mA cm^{-2}, and FF of 64.22%. The multi-layer stack configuration of this device may introduce additional interfacial impedance and hinder carrier transportation, leading to a reduction in FF from 71.19% to 64.22% compared to the device with the configuration of Glass/OPV/Glass. However, the increasing J_{sc} of the top-illuminated devices suggests that the alternative top electrode of WO_3/Ag/MoO_3 may exhibit good transparency or conductivity comparable to that of ITO. We further peeled the devices deposited on the parylene and measured the PCE of the flexible top-illuminated devices resulting in a PCE is 8.75%, with a V_{oc} of 0.81 V, a J_{sc} of 17.84 mA cm^{-2}, and an FF of 60.08%. The EQE spectrum of these devices are shown in Fig. 4b, where the EQE profiles and simulated J_{sc} from EQE are consistent with the transmittance results and *J–V* curves of the devices. Fig. 4c depicts the peeling process, with a detailed visual representation available in the accompanying supplementary video (S2, ESI†). The standalone peeling devices (Device 3) exhibit a PCE similar to that of Device 2, indicating that the devices retain good structural integrity after peeling and are not damaged during the peeling process. In addition, the total thickness and weight of the crumpled OPV are approximately 2.0 μm and 1.5 mg respectively, resulting in an impressive high power-per-weight of 31.07 W g^{-1}. The detailed calculation of the power-per-weight of all the synthesized devices are presented in the ESI† (S1).

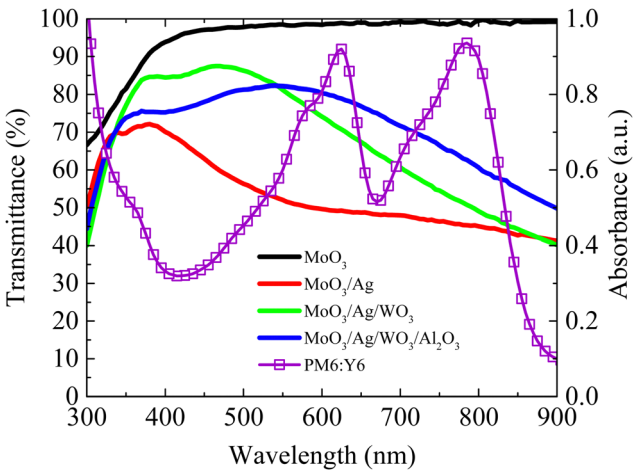

Fig. 5 The transmittance spectra and absorption coefficient for MoO_3, MoO_3 (10 nm)/Ag (12 nm), MoO_3 (10 nm)/Ag (12 nm)/WO_3 (30 nm), MoO_3 (10 nm)/Ag (12 nm)/WO_3 (30 nm)/Al_2O_3 (30 nm) and PM6:Y6 observed across the wavelength range from 300 to 900 nm.

Fig. 5 illustrates the variation in the transmittance of different devices of MoO_3 (10 nm)/Ag (12 nm), MoO_3 (10 nm)/Ag (12 nm)/WO_3 (30 nm), and MoO_3 (10 nm)/Ag (12 nm)/WO_3 (30 nm)/Al_2O_3 (30 nm) as well as the absorption coefficient for the active layer of PM6:Y6. The absorption region of the active layer (PM6:Y6) primarily spans 400–850 nm, with absorption peaks for PM6 and Y6 located at approximately 600 nm and 800 nm, respectively. Pristine MoO_3 (10 nm) demonstrates a high transmittance of 95% and the deposition of a 12 nm thin Ag layer significantly reduces the transmittance to 50% due to metal scattering. Incorporating a 30 nm WO_3 layer as a resonance cavity, increases the transmittance within this range to approximately 70%. Furthermore, depositing an additional 30 nm Al_2O_3 layer can further enhance the overall transmittance, reaching 80%. It is important to note that, despite offering advantages over ITO electrodes, this alternative electrode exhibits a modest reduction approximately 10% transmittance. However, while the MoO_3/Ag/WO_3 alternative electrode may exhibit a lower sheet resistance of 5.35 Ω □$^{-1}$, compared to the resistance of ITO electrodes, which is typically 15 Ω □$^{-1}$. This low sheet resistance is a substantial advantage as it enhances carrier conduction and collection efficiency, effectively compensating for the limitations in transmittance associated with alternative electrodes.

We conducted stability tests on the relevant devices, which included evaluations under both dark and light illumination conditions. The results of the stability test under dark conditions are presented in Fig. 6. Remarkably, the PCE of the Device 2 remained nearly unchanged even after 1000 hours of storage in a dark environment. However, comparing the devices with

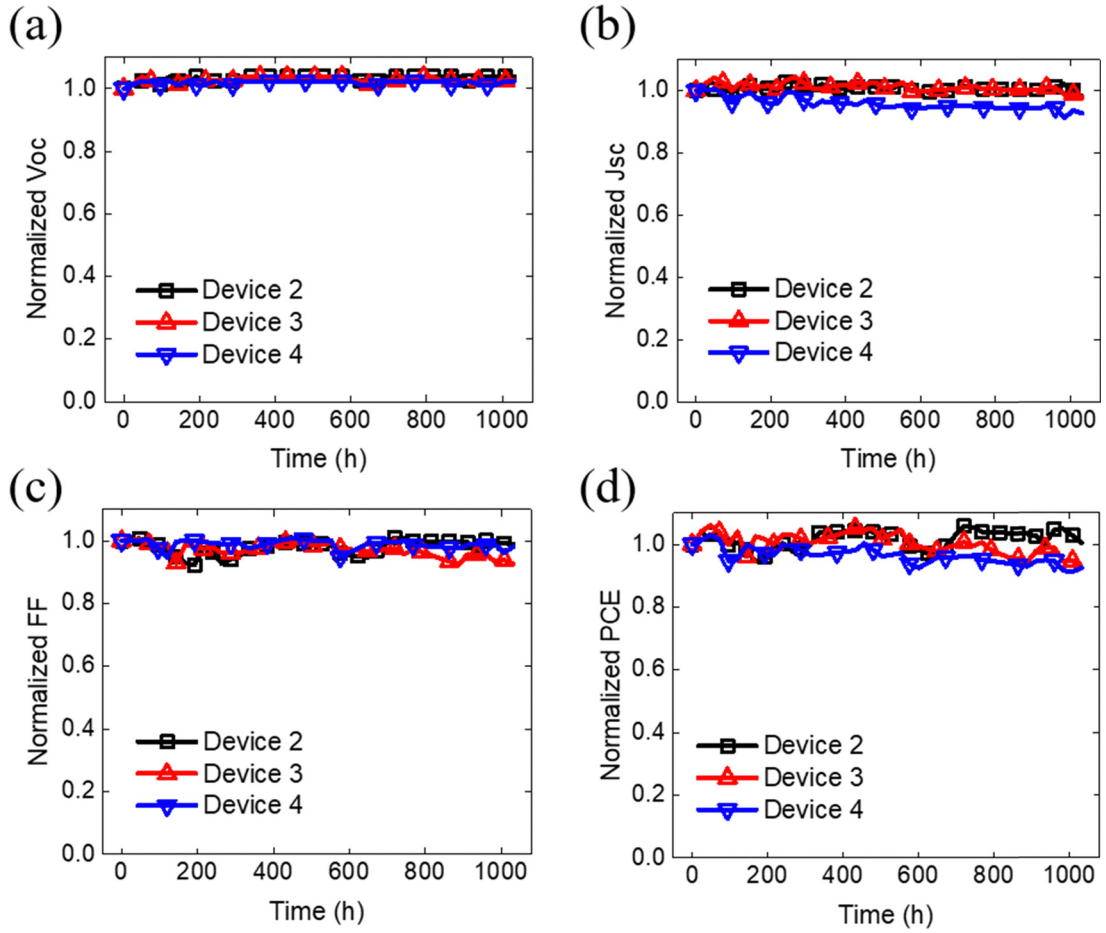

Fig. 6 The environmental stability testing for our proposed OPVs under dark conditions. (a) Open circuit voltage (V_{oc}), (b) short circuit current density (J_{sc}), (c) fill factor (FF), and (d) power conversion efficiency (PCE) observed at various time intervals.

Glass/OPV/Glass and crumpled OPVs a reduction in efficiency by 5% was seen. Notably, the V_{oc} of these devices was not affected during 1000 hours of storage in a dark environment indicating that the reduction in 5% PCE was primarily attributed to the respective decreasing J_{sc} and FF. Furthermore, the evaluation was conducted under an LED lamp with an illumination of 100 mW cm^{-2}. Fig. 7, demonstrate the V_{oc} remained at the stable over 96 h under light conditions. However, the photovoltaic characteristics mainly affected by light condition, resulting in low J_{sc} and FF, due to probable high-energy photons inducing photodecomposition of NFA degradation.[45] After subjecting the device to 96 h of light exposure, both Device 4 and Device 2 devices managed to retain about 90% of their initial PCE. This result indicates that the deposition of Al_2O_3 by ALD can effectively protect the underneath organic films, which is consistent with previous literature reports.[46,47]

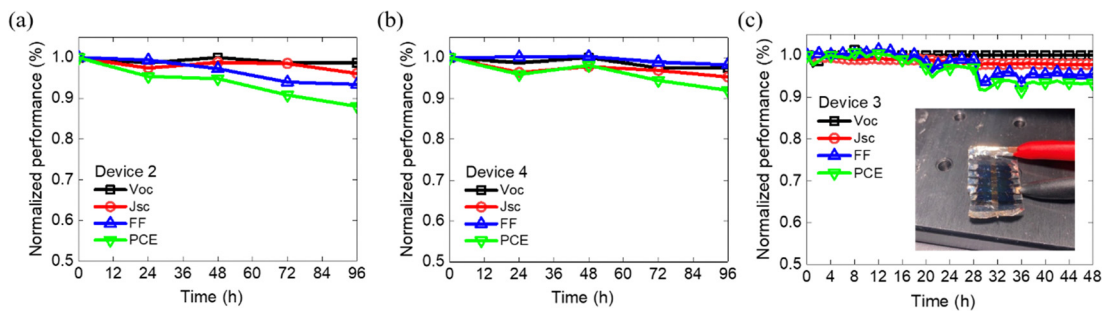

Fig. 7 Device performance *vs.* operation time for the device configurations of (a) Device 2 and (b) Device 4 under one sun illumination with 96 h. (c) Device performance *vs.* operation time for our proposed lightweight device and Device 3 under one sun illumination. After 48 h, the proposed device maintains its PCE with T93 comparable to the fresh device.

Notably, Device 2 exhibited more severe FF degradation compared to Device 4, suggesting the potential for significant carrier accumulation at the interfacial layer between the OPV layer and Al_2O_3 under prolonged light exposure. Finally, our crumpled OPV devices, maintaining 93% of the initial PCE value after 48 hours of light illumination. This excellent performance highlights the potential of the crumpled OPV devices for enhancing OPV durability and longevity.

Conclusions

A top-illuminated ITO-free crumpled OPV structure was prepared with an ITO-free alternative, utilizing a flexible parylene substrate. In this device design, a polymer PFN-Br was chosen as the ETL to achieve a flexible and lightweight goal. The traditional ITO transparent electrode was replaced with the MoO_3/Ag/WO_3 as an alternative transparent electrode. This device demonstrated an increase in J_{sc}, indicating improved transparency and conductivity comparable to ITO. Moreover, the MoO_3/Ag/WO_3 alternative electrode offers a lower sheet resistance of 5.35 Ω $\square^{-1}$, outperforming the 15 Ω $\square^{-1}$ sheet resistance of ITO. The strong absorption observed in the PN6A film, especially at a wavelength of 900 nm, suggests the rearrangement of the PM6 and Y6 mixture during thermal annealing. This strong absorption and advantageous low sheet resistance enhances carrier conduction and collection efficiency, effectively compensating for any potential stability concerns of the device. Device 2 exhibits a PCE similar to that of Device 3, indicating that it retains a robust structure and is not negatively influenced by the peeling process. Additionally, the total thickness and weight of the crumpled OPV are approximately ∼2 μm and 1.5 mg, respectively and it boasts remarkable characteristics with a power-per-weight of up to 31.07 W g^{-1} and exhibits remarkable stability during dark storage (T95 ∼ 1000 hours) and light soaking (T93 ∼ 48 hours).

Conflicts of interest

The authors declare no conflict of interest.

Acknowledgements

This work was supported by the National Science and Technology Council, Taiwan, under Grant No. NSTC 111-2923-E-002-012-MY3; NSTC 112-2622-E-131-001; NSTC 112-2628-E-131-001-MY4; NSTC 112-2221-E-131-021; and NSTC 112-2622-E-131-006.

References

1 X. Zheng, L. Zuo, K. Yan, S. Shan, T. Chen, G. Ding, B. Xu, X. Yang, J. Hou and M. Shi, *Energy Environ. Sci.*, 2023, **16**, 2284–2294.
2 M. M. Ovhal, H. B. Lee, S. Boud, K.-J. Ko, W.-Y. Jin, N. Kumar, B. Tyagi and J.-W. Kang, *Mater. Today Energy*, 2023, **34**, 101289.
3 K. Fukuda and T. Someya, presented in part at the 2022 29th International Workshop on Active-Matrix Flatpanel Displays and Devices (AM-FPD), Japan, 5–8 July 2022, 2022.
4 H.-C. Cha, Y.-C. Huang, F.-H. Hsu, C.-M. Chuang, D.-H. Lu, C.-W. Chou, C.-Y. Chen and C.-S. Tsao, *Sol. Energy Mater. Sol. Cells*, 2014, **130**, 191–198.
5 E. Ravishankar, R. E. Booth, C. Saravitz, H. Sederoff, H. W. Ade and B. T. O'Connor, *Joule*, 2020, **4**, 490–506.
6 D. Han, S. Han, Z. Bu, Y. Deng, C. Liu and W. Guo, *Sol. RRL*, 2022, **6**, 2200441.
7 P. Bi, J. Ren, S. Zhang, J. Wang, Z. Chen, M. Gao, Y. Cui, T. Zhang, J. Qin, Z. Zheng, L. Ye, X. Hao and J. Hou, *Nano Energy*, 2022, **100**, 107463.
8 B. Lee, L. Lahann, Y. Li and S. R. Forrest, *Sustainable Energy Fuels*, 2020, **4**, 5765–5772.
9 Y. Huang, D. Lu, C. Li, C. Chou, H. Cha and C. Tsao, *IEEE J. Photovolt.*, 2019, **9**, 1297–1301.
10 S.-Y. Chuang, H.-L. Chen, W.-H. Lee, Y.-C. Huang, W.-F. Su, W.-M. Jen and C.-W. Chen, *J. Mater. Chem.*, 2009, **19**, 5554–5560.
11 X. Yuan, Y. Zhao, D. Xie, L. Pan, X. Liu, C. Duan, F. Huang and Y. Cao, *Joule*, 2022, **6**, 647–661.
12 Q. Liu, Y. Jiang, K. Jin, J. Qin, J. Xu, W. Li, J. Xiong, J. Liu, Z. Xiao, K. Sun, S. Yang, X. Zhang and L. Ding, *Sci. Bull.*, 2020, **65**, 272–275.
13 A. Shang, S. Luo, J. Zhang, H. Zhao, X. Xia, M. Pan, C. Li, Y. Chen, J. Yi and X. Lu, *Sci. China: Chem.*, 2022, **65**, 1758–1766.
14 L. Hong, H. Yao, R. Yu, Y. Xu, B. Gao, Z. Ge and J. Hou, *ACS Appl. Mater. Interfaces*, 2019, **11**, 29124–29131.
15 L. Zhu, M. Zhang, J. Xu, C. Li, J. Yan, G. Zhou, W. Zhong, T. Hao, J. Song, X. Xue, Z. Zhou, R. Zeng, H. Zhu, C.-C. Chen, R. C. I. MacKenzie, Y. Zou, J. Nelson, Y. Zhang, Y. Sun and F. Liu, *Nat. Mater.*, 2022, **21**, 656–663.
16 Y. Yu, J. Nassar, C. Xu, J. Min, Y. Yang, A. Dai, R. Doshi, A. Huang, Y. Song and R. Gehlhar, *Sci. Robot.*, 2020, **5**, eaaz7946.
17 D. Verma, K. R. Singh, A. K. Yadav, V. Nayak, J. Singh, P. R. Solanki and R. P. Singh, *Biosens. Bioelectron.: X*, 2022, **11**, 100153.
18 F. Wu, C. Rüdiger and M. R. Yuce, *Sensors*, 2017, **17**, 282.
19 M. N. Boukoberine, T. Donateo and M. Benbouzid, *IEEE Trans. Energy Convers.*, 2022, **37**, 2080–2091.
20 K. Chen and Z. Zhang, *IEEE Ind. Electron. Mag.*, 2023, 2–12.
21 J. Jean, A. Wang and V. Bulović, *Org. Electron.*, 2016, **31**, 120–126.
22 H. Kimura, K. Fukuda, H. Jinno, S. Park, M. Saito, I. Osaka, K. Takimiya, S. Umezu and T. Someya, *Adv. Mater.*, 2019, **31**, 1808033.
23 T. Y. Qu, L. J. Zuo, J. D. Chen, X. Shi, T. Zhang, L. Li, K. C. Shen, H. Ren, S. Wang and F. M. Xie, *Adv. Opt. Mater.*, 2020, **8**, 2000669.
24 T. Chen, S. Li, Y. Li, Z. Chen, H. Wu, Y. Lin, Y. Gao, M. Wang, G. Ding and J. Min, *Adv. Mater.*, 2023, 2300400.
25 Z. Zheng, J. Wang, P. Bi, J. Ren, Y. Wang, Y. Yang, X. Liu, S. Zhang and J. Hou, *Joule*, 2022, **6**, 171–184.

26 S. Xiong, K. Fukuda, S. Lee, K. Nakano, X. Dong, T. Yokota, K. Tajima, Y. Zhou and T. Someya, *Adv. Sci.*, 2022, **9**, 2105288.
27 W. Song, K. Yu, E. Zhou, L. Xie, L. Hong, J. Ge, J. Zhang, X. Zhang, R. Peng and Z. Ge, *Adv. Funct. Mater.*, 2021, **31**, 2102694.
28 F. Barlow, M. A. Naby, A. Joshi and A. Elshabini-Riad, *Sol. Energy Mater Sol. Cells*, 1994, **33**, 63–71.
29 M. Al-Kuhaili, *J. Mater. Sci.: Mater. Electron.*, 2020, **31**, 2729–2740.
30 B. Azzopardi, C. J. Emmott, A. Urbina, F. C. Krebs, J. Mutale and J. Nelson, *Energy Environ. Sci.*, 2011, **4**, 3741–3753.
31 Z. Chen, B. Cotterell, W. Wang, E. Guenther and S.-J. Chua, *Thin Solid Films*, 2001, **394**, 201–205.
32 Y. H. Kim, C. Sachse, M. L. Machala, C. May, L. Müller-Meskamp and K. Leo, *Adv. Funct. Mater.*, 2011, **21**, 1076–1081.
33 S. R. Ha, S. Park, J. T. Oh, D. H. Kim, S. Cho, S. Y. Bae, D.-W. Kang, J.-M. Kim and H. Choi, *Nanoscale*, 2018, **10**, 13187–13193.
34 M. G. Kang, T. Xu, H. J. Park, X. Luo and L. J. Guo, *Adv. Mater.*, 2010, **22**, 4378–4383.
35 Z. Yu, L. Li, Q. Zhang, W. Hu and Q. Pei, *Adv. Mater.*, 2011, **23**, 4453–4457.
36 S. I. Na, S. S. Kim, J. Jo and D. Y. Kim, *Adv. Mater.*, 2008, **20**, 4061–4067.
37 D. Koo, S. Jung, J. Seo, G. Jeong, Y. Choi, J. Lee, S. M. Lee, Y. Cho, M. Jeong, J. Lee, J. Oh, C. Yang and H. Park, *Joule*, 2020, **4**, 1021–1034.
38 Y. Wang, S. W. Tong, X. F. Xu, B. Özyilmaz and K. P. Loh, *Adv. Mater.*, 2011, **23**, 1514–1518.
39 C.-Y. Chang, Y.-C. Chang, W.-K. Huang, W.-C. Liao, H. Wang, C. Yeh, B.-C. Tsai, Y.-C. Huang and C.-S. Tsao, *J. Mater. Chem. A*, 2016, **4**, 7903–7913.
40 G. Kumar, S. Biring, Y.-N. Lin, S.-W. Liu and C.-H. Chang, *Org. Electron.*, 2017, **42**, 52–58.
41 C. Zhang, C. Ji, Y. B. Park and L. J. Guo, *Adv. Opt. Mater.*, 2021, **9**, 2001298.
42 B. O'Connor, C. Haughn, K.-H. An, K. P. Pipe and M. Shtein, *Appl. Phys. Lett.*, 2008, **93**, 223304.
43 Y. G. Bi, Y. F. Liu, X. L. Zhang, D. Yin, W. Q. Wang, J. Feng and H. B. Sun, *Adv. Opt. Mater.*, 2019, **7**, 1800778.
44 H.-C. Kwon, W. Jeong, Y.-S. Lee, J.-H. Jang, H.-S. Jeong, S. Kim, D. Song, A. Park, E. Noh, K. Lee and H. Kang, *Adv. Energy Mater.*, 2022, **12**, 2200023.
45 T. Liu, Q. C. Burlingame, M. R. Ivancevic, X. Liu, J. Hu, B. P. Rand and Y.-L. Loo, *Adv. Energy Mater.*, 2023, **13**, 2300046.
46 S.-H. Ko Park, J.-Y. Oh, C.-S. Hwang, Y.-S. Yang, J.-I. Lee and H.-Y. Chu, *J. Inf. Disp.*, 2004, **5**, 30–34.
47 J. Wu, F. Fei, C. Wei, X. Chen, S. Nie, D. Zhang, W. Su and Z. Cui, *RSC Adv.*, 2018, **8**, 5721–5727.